MDPI

Article

Operando Analysis of Losses in Commercial-Sized Solid Oxide Cells: Methodology Development and Validation

Antunes Staffolani [1,*], Arianna Baldinelli [2], Gianni Bidini [2,*], Francesco Nobili [1] and Linda Barelli [2]

1   School of Science and Technologies, Chemistry Division, Via Madonna delle Carceri ChIP, Università di Camerino, I-62032 Camerino, Italy; francesco.nobili@unicam.it
2   Department of Engineering, Università degli Studi di Perugia, Via Duranti 93, I-06125 Perugia, Italy; arianna.baldinelli@unipg.it (A.B.); linda.barelli@unipg.it (L.B.)
*   Correspondence: antunes.staffolani@unicam.it (A.S.); gianni.bidini@unipg.it (G.B.)

Abstract: The development of decarbonised systems is being fostered by the increasing demand for technological solutions for the energy transition. Solid Oxide Cells are high-efficiency energy conversion systems that are foreseen for commercial development. They exhibit potential power generation and power-to-gas applications, including a reversible operation mode. Long-lasting high performance is essential for guaranteeing the success of the technology; therefore, it is fundamental to provide diagnosis tools at this early stage of development. In this context, operando analysis techniques help detect and identify incipient degradation phenomena to either counteract damage at its origin or correct operando protocols. Frequent switches from the fuel cell to the electrolyser mode add more challenges with respect to durable performance, and deep knowledge of reverse-operation-induced damage is lacking in the scientific and technical literature. Following on from preliminary experience with button cells, in this paper, the authors aim to transfer the methodology to commercial-sized Solid Oxide Cells. On the basis of the experimental evidence collected on planar square cells under dry and wet reactant feed gases, the main contributions to impedance are identified as being charge transfer ($f = 10^3$–10^4 Hz), oxygen surface exchanged and diffusion in bulk LSCF ($f = 10^2$–10^3 Hz), and gas diffusion in the fuel electrode (two peaks, $f = 1$–100 Hz). The results are validated using the ECM methodology, implementing an LRel(RctQ)GWFLW circuit.

Keywords: solid oxide fuel cells; ElS; DRT; equivalent circuit model; operando

1. Introduction

The clean energy transition boasts new efficient and decarbonised energy conversion and storage solutions [1]. In this roadmap, hydrogen and fuel cells are considered to be game-changing technologies [2]. In this context, Solid Oxide Cells (SOCs) deserve attention for their capacity for reverse operation, both as power generators (SOFC, fuel cell operation mode) and power-to-gas technology (SOE, electrolyser operation mode) [3]. SOCs run at a higher temperature level (650–850 °C) than other fuel cell and electrolysis technologies. From a thermodynamic point of view, this represents an advantage in terms of efficiency. Regarding alkaline and polymeric membrane cells used for electrolysis purposes, SOCs score +30% efficiency [4] thanks to favourable thermodynamic conditions (Figure 1, right). Higher temperature is a crucial factor for improving electrochemistry kinetics and electrical properties. The efficiency gain in fuel cell operation is not as high; however, higher temperature makes it possible to use heterogeneous fuel mixtures.
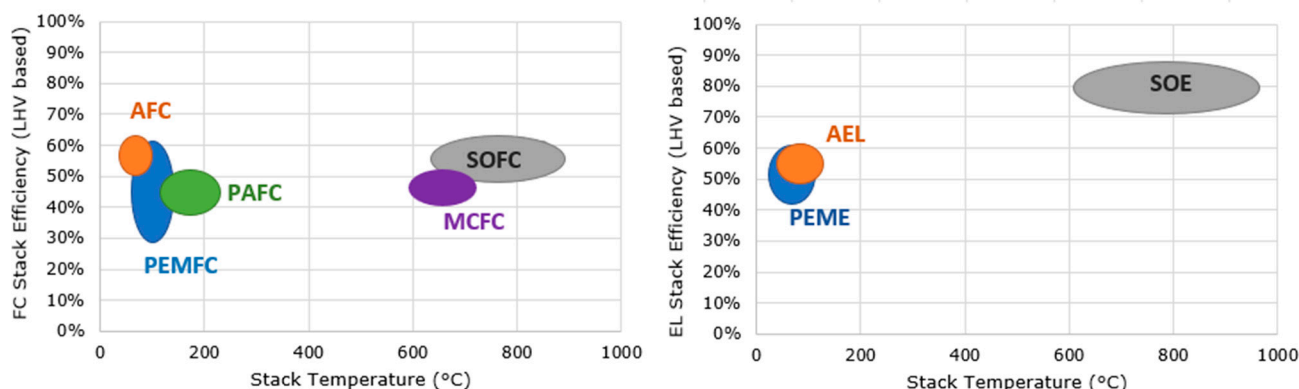
Figure 1. Fuel cells (**left**) and electrolysers (**right**): stack efficiency vs. operative temperature [4] for alkaline electrolysers (AEL) alkaline fuel cells (AFC), molten carbonate fuel cells (MCFC), phosphoric acid fuel cells (PAFC), polymer membrane electrolysis membranes (PEME), polymer membrane fuel cells (PEMFC), solid oxide electrolysers (SOE), solid oxide fuel cells (SOFC).

Nonetheless, higher temperatures counteract the achievement of long-lasting lifetimes for individual devices. From a macroscopic point of view, higher temperature levels can cause thermomechanical stress and differential volume variation in ceramic and metallic parts. Additionally, looking at micro-structural issues, high temperatures can even cause physiological decay, which can mainly be ascribed to catalyst sintering and redox cycles [5]. In addition to thermally induced damage, other operating conditions affect the lifetime. The reversible operation mode (fuel cell/electrolyser) requires hydrogen and water steam to be fed into the SOC unit inlets. On the one hand, the fuel electrode is fed with hydrogen in power generation mode (fuel cell), achieving a reducing atmosphere in the SOC's anode compartments (this helps prevent the re-oxidation of the catalysts, mostly Nickel). On the other hand, the operation in power-to-gas mode calls for a water steam feeding, which creates oxidising conditions onto the same materials. The water steam feeding is enriched with hydrogen to prevent fast oxidation.

Lifetime is a crucial indicator for the technology's success and boosts the commercial stage of development. It is necessary to fully understand the impact of the real operation on SOC materials. Therefore, temperature and feeding gases effects on electrodes must be monitored during SOC working cycles without interfering with the regular operation. Electrochemical impedance spectroscopy (EIS) and related deconvolution by the Distribution of Relaxation Times (DRT) method are powerful tools beyond the standard characterisation of electrochemical cells through the polarisation test. Thanks to DRT, it is possible to gain insight into single processes determining power losses, such as reaction kinetics and transport phenomena. Since EIS is a non-destructive technique, it can be applied as in operando characterisation, without the need for either stopping operation or complex measuring systems, as in the case of spectroscopy characterisations (i.e., Raman, XRD [6]). For this reason, it is highly impactful in the analysis of progressive degradation of the electrodes and the electrolyte. DRT is a model-free representation of the AC response of the system under study and, in particular, a comparative method (i.e., to properly correlate DRT peaks to charge transfer and transport phenomena, a comparison study with different operating conditions needs to be carried out). For instance, in SOCs, the evolution of the intensity and the relaxation time of the DRT peaks is commonly studied under different working temperatures, current load, and gas flow rates and compositions [7]. In the case of Li-ion batteries, the DRT profile is commonly studied at different state-of-charge values [8–10], while on solar cells, it is examined under different light irradiation levels [11,12].

In the context of Solid Oxide Cells, this research thread was initiated by scientists from the Karlsruhe Institute of Technology with some milestone works [13] more than a decade ago. Since then, this technique has been implemented in several other papers. More recently, Osinkin [14] published a further paper with EIS-DRT investigation on planar

Pt/YSZ/LSM cells operated at 850 °C fed with different gas mixtures (air or Ar + O_2 at the Air Electrode -AE-, humidified Ar + H_2 at the Fuel Electrode-FE-). The technique is also applied in the recent work by Sumi et al. [15] to measure electrodes degradation in microtubular SOFCs operated at 600–650 °C. Sumi et al. observed: (i) the increase in the polarisation resistance of charge transfer and ionic conduction processes in the FE, as a result of a rapid coarsening of Ni grains, (ii) the increase of oxygen surface exchange and diffusion processes in the AE, caused by the slow growth of LSC. EIS and DRT find further application in measuring cells degradation in stacks. Results to this end were reported by Yan et al. [16] (NiYSZ/YSZ/LSCF cells stack), Subotic et al. [17] (Ni-GDC/YSZ/LSCF cells stack). All the past studies concerning SOFCs advanced characterisation by EIS + DRT contributed to the knowledge about identifying loss mechanisms.

EIS responses are commonly approximated by complex non-linear least square fit (CNLS) using a proper equivalent circuit model (ECM). However, due to the system's complexity, resulting from porous electrodes with a mosaic microstructure, the choice of a representative ECM implies a priori knowledge of the system under study, and the CNLS-fit is not easy as in standard CNLS-fitting routines. Furthermore, more than one ECM can provide fits of the same quality, even without any physicochemical meaning. In addition, impedance responses are commonly displayed in Nyquist or Bode plots, in which features with close relaxation frequencies or time constants are not discernible. To gain a deeper insight into the EIS responses, it is helpful to deconvolute the obtained spectra into their components according to their characteristic time, therefore determining the DRT function. DRT is a well-established technique for the deconvolution of impedance spectra [18] and can be estimated by various methods, such as maximum entropy [19,20], Fourier transform [21,22], Tikhonov regularisation [23–25] and multiple-(RQ) fit developed by Boukamp with CNLS methodology [26]. In the case of Fourier transform, a window function must be applied, which dramatically affects the shape of the DRT function. In the case of maximum entropy and Tikhonov regularisation, a "special parameter" must be optimised to avoid under- (smooth curve with fewer peaks) or over-estimation (overinterpretation with the creation of artefact peaks) of the DRT function. EIS responses of SOC in fuel cell mode are commonly acquired in the frequency range 0.1 mHz < f < 10 kHz. A summary of the possible peak attributions is reported in Table 1 [13,27–30].

Table 1. Literature survey of possible peak attribution.

Ref	$f < 1$ Hz	1 Hz < f < 10 Hz	10 Hz < f < 100 Hz	0.1 kHz < f < 0.5 kHz	0.5 kHz < f < 100 kHz	5 kHz < f < 200 Hz
[27]	Conversion diffusion at low pO_2 transport in reforming mixture	Gas conversion	Fuel electrode diffusion/oxygen electrode reaction + solid state diffusion	Secondary peaks (fuel and oxygen electrode transport)	Fuel electrode charge transfer	Unidentified high-frequency peak
Dependencies	pO_2	$F_{tot} > pH_2 > i > pO_2 > T$	$pH_2O > i > F_{tot} > pO_2 > T$	$pH_2O > T > pO_2$	$T > I > pH_2O$	T
	0.1 Hz < f < 1 Hz	**1 Hz < f < 10 Hz**	**10 Hz < f < 100 Hz**	**0.1 kHz < f < 1 kHz**	**1 kHz < f < 100 kHz** **5 kHz < f < 200 Hz**	
[28]	Gas diffusion or polarisation at the air electrode	Air electrode gas diffusion (low pO_2) or surface reaction on the cathode (high pO_2)	Fuel electrode gas diffusion (low pH_2O) or surface reaction on the fuel electrode		Bulk or surface diffusion at the fuel electrode	
Dependencies	pO_2	pO_2	pH_2O			
	0.1 Hz < f < 1 Hz	**1 Hz < f < 50 Hz**	**10 Hz < f < 100 Hz**		**0.5 kHz < f < 10 kHz**	
[7,13,29]	Gas diffusion in the cathode (including contact mesh and flowfield)	Gas diffusion in the anode substrate (including contact mesh and flowfield)	Oxygen surface exchange kinetics & bulk diffusion of O^{2-}		Charge transfer coupled to gas diffusion and ionic transport.	
Dependencies	pO_2, T, j	pH_2, pH_2O, T, j	pO_2, T, j		T, pH_2, pH_2O, T	

In this context, this paper aims to further develop a methodology for the identification of early-stage degradation effects in commercial-sized SOCs and to validate with respect to SOC applications under relevant operating conditions (squared-area cells + steel interconnection frames). To this end, the paper firstly highlights the experimental evidence, namely impedance sensitivity to operating conditions. This step is fundamental to identifying physico-chemical phenomena behind performance losses (i.e., charge transfer, gas diffusion). Thereby, the paper shows a systematic approach to obtaining the ECM of the SOC in variable operating conditions. The experimental characterization covers a broad domain of conditions, including a wide temperature range (640–820 °C), different oxygen partial pressures at the AE (5–21%$_{vol}$), as well as variable hydrogen (7–97%$_{vol}$), and water steam (3–50%$_{vol}$) partial pressures at the FE. The operating variables are combined to explore synergistic effects of FE and AE feeding on the overall cell impedance. As a result of the empirical correlation between the process variables and the DRT signal peaks, it is possible to detect the evolution of each functional part (i.e., electrolyte, anodic/cathodic catalyst, anodic/cathodic gas diffusion layer) to the overall impedance and, therefore, to attribute to a specific part the cause of performance decay. Consequently, this study contributes significantly to building a diagnostic tool based on the DRT signal analysis for the in operando monitoring of the SOC state-of-health. Upon completion of its development, the diagnostic tool is meant to be applied in reversible SOCs (rSOCs), allowing a detailed investigation of performance decay in real operating conditions and as the effect of commutation in the reversible operation cycles—storage charging and discharging phases. The developed diagnostic tool will be periodically applied to the fuel cell operation mode, so after a certain number of commutation cycles.

2. Materials and Methods

In this section, the preparation of the experimental activity is described, with an overview of materials and measurement instruments (Section 2.1), methods (Section 2.2), and details of the test campaign (Section 2.3).

2.1. Materials

The experiments are executed on commercial planar anode-supported NiYSZ/8YSZ/ GDC-LSCF cells, using samples with a square geometry (side 5 cm, overall thickness < 0.3 mm). Cells are installed in a gas-tight AISI40 steel housing consisting of three parts, the fuel electrode manifold, the intermediate frame plate and the air electrode manifold (Figure 2). Steel components exposed to an oxidant atmosphere are coated with $CuMn_2O_4$ to preserve the active surfaces from Cr evaporation [30]. Gas tightness is achieved with a two-layer sealing made of a mineral core (Spetech Spetoterm, Bielsko-Biala, Poland) and a glass-ceramic paste (SCHOTT G018-354, Schott AG, Mainz, Germany). Electric contact is assured by Ni and Au meshes at the fuel and air sides, realising an active area of 16 cm^2.
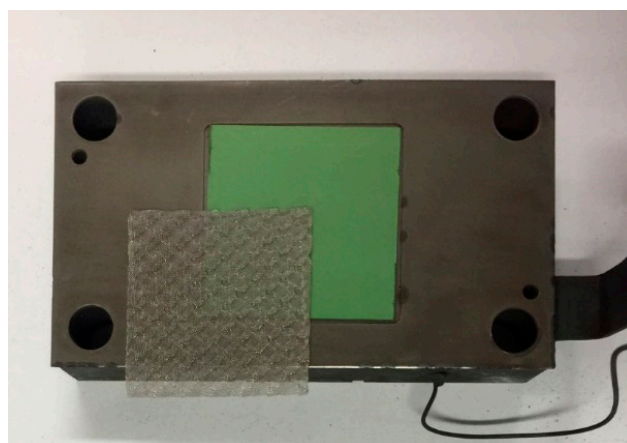

Figure 2. Commercial-sized SOFC: setup with a metal housing and a Ni current collector mesh.

The housing is placed in an electric furnace equipped with a temperature control system. Feeding gas lines are supplied with technical-purity hydrogen and nitrogen, compressed atmospheric air and deionised water. Gas flow rates are controlled by digital mass flow meters, while water steam is regulated with a temperature-controlled bubbler. Reversible operation is managed by an electronic system made of a controller (Arduino) plus an electronic load. Online electrochemical impedance (EIS) measurements are accomplished with a potentiostat (Biologic SP-240, ranges: current 4 A, voltage 2 V). A descriptive scheme of the test rig and related instruments is provided in Figure 3.
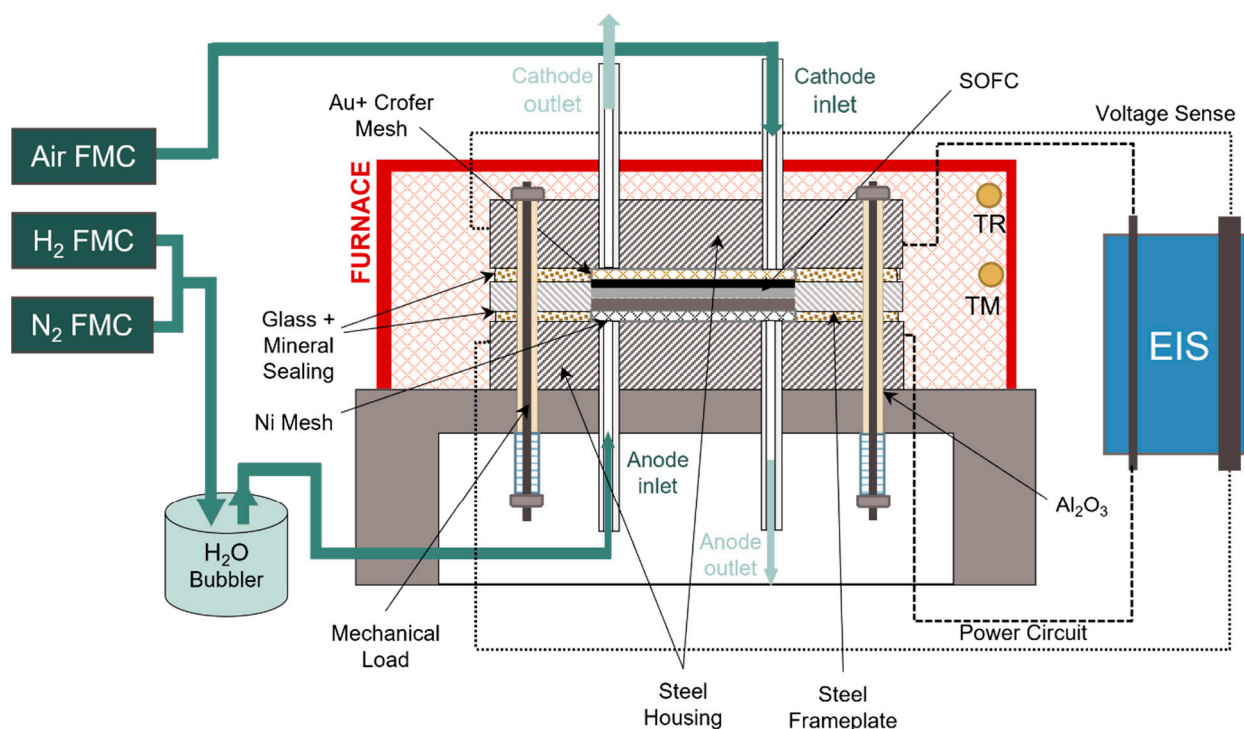

Figure 3. SOFC test rig scheme: mechanical and electrical connection, measurement hardware.

2.2. Methods

EIS is periodically acquired during each test to have a complete overview of performance evolution. The EIS scans are performed in galvanostatic mode with a 350-mA-amplitude current wave. The EIS scan begins at 100 kHz and ends at 100 mHz (12 ppd resolution with logarithmic spacing). Each measurement is the result of an average of 5 samples. EIS is measured under two feeding conditions of the FE: (i) hydrogen/water equimolar (at 0 A, 3.5 A, and −3.5 A), and (ii) dry hydrogen (at 0 A and −3.5 A) streams. The full methodology is detailed in a previous paper published by the authors [31]. All the impedance data elaborations are carried out using the Relaxis 3 software from rhd instruments. The quality of the AC responses is assessed by analysing the residuals from the Kramers–Kronig test. Then, the DRT function is calculated through the Tikhonov regularisation. To avoid under- or overestimation of the DRT function, an optimization of the regularization parameter needs to be carried out. Thus, the DRT function is calculated with λ equal to 10^{-1}, 10^{-2}, 10^{-3}, and 10^{-4}. The Nyquist plots are reconstructed from the obtained DRT, then both residuals $\Delta_{re}(\omega_i)$ and $\Delta_{im}(\omega_i)$ (Equations (1) and (2) [21]), as well as pseudo χ^2 (Equation (3)) are calculated comparing the experimentally measured impedance with the DRT-obtained one.

$$\Delta_{re}(\omega_i) = \frac{Z_{dat,re}(\omega_i) - Z_{DRT,re}(\omega_i)}{|Z_{dat}(\omega_i)|} \qquad (1)$$

$$\Delta_{im}(\omega_i) = \frac{Z_{dat,im}(\omega_i) - Z_{DRT,im}(\omega_i)}{|Z_{dat}(\omega_i)|} \tag{2}$$

$$\chi^2_{DRT} = \frac{1}{N}\sum_N \frac{(Z_{dat,re}(\omega_i) - Z_{DRT,re}(\omega_i))^2 + (Z_{dat,im}(\omega_i) - Z_{DRT,im}(\omega_i))^2}{|Z_{dat}(\omega_i)|} \tag{3}$$

At last, the sum of squared residuals vs. λ is calculated. The inductive feature in the high-frequency region is fitted for the DRT calculation.

2.3. Equivalent Circuit Model and Data Fit

The entire CNLS fit procedure is carried out with Relaxis 3 software (rhd instruments). An equivalent circuit model comprising LR(RC)GW$_{FLW}$ (written in Boukamp's notation [32], shown in Figure 8a) is used to fit the impedance spectra. A further (RC) can be added when fitting impedance spectra acquired with a xO$_2$ << 21% in the air electrode. All the capacitor elements are replaced with a constant phase element (Q) to consider electrode roughness and inhomogeneities [33]. The CNLS fit is refined until $\chi^2 \approx 10^{-6}$–10^{-7} is reached.

2.4. Test Campaign

Due to the need to retrieve experimental data in several operating conditions, the test campaign is planned as shown in Table 2, and then Table 3 shows the test plan with a focus on temperature variation (600–800 °C). For this test series, the reactant gas concentrations and total flow rate do not vary, and the current density levels are standard (0 and 100 mA/cm^2). In particular, Table 2 shows all the tests interested in the variation of reactant gas partial pressures obtained by mixing the desired gases in a given proportion in volume. On the one hand, hydrogen concentration varies in the range 7–97% when water steam is added in accordance with ambient temperature conditions (therefore, with a concentration of 3%$_{vol}$). At the same time, the modulation is narrower when hydrogen is balanced with a higher amount of water steam (up to 50%$_{vol}$). On the other hand, the oxygen concentration is decreased from the typical amount in ambient air, down to 5%$_{vol}$. Temperature is set to 750 °C for all tests presented in Table 2, while current density is set to 0 and 100 mA/cm^2.

Table 2. Design of experiments—part 1 "electrode feeding gas variation".

T	FE Supply				AE Supply			Operating Currents	
	$\dot{Q}$	x_{H_2}	x_{N_2}	x_{H_2O}	$\dot{Q}$	x_{O_2}	x_{N_2}	j0	j1
°C	NL/h	%$_{vol,wb}$	%$_{vol,wb}$	%$_{vol,wb}$	NL/h	%$_{vol,db}$	%$_{vol,db}$	mA/cm^2	mA/cm^2
750	50	97.0%	0%	3%	50	21%	79%	0	100
750	50	48.5%	48.5%	3%	50	21%	79%	0	100
750	50	24.3%	72.8%	3%	50	21%	79%	0	100
750	50	97.0%	0%	3%	50	10%	90%	0	100
750	50	48.5%	48.5%	3%	50	10%	90%	0	100
750	50	24.3%	72.8%	3%	50	10%	90%	0	100
750	50	97.0%	0%	3%	50	5%	95%	0	100
750	50	48.5%	48.5%	3%	50	5%	95%	0	100
750	50	24.3%	72.8%	3%	50	5%	95%	0	100
750	50	75%	0%	25%	50	21%	79%	0	100
750	50	75%	0%	25%	50	10%	90%	0	100
750	50	75%	0%	25%	50	5%	95%	0	100
750	50	50%	0%	50%	50	21%	79%	0	100
750	50	50%	0%	50%	50	10%	90%	0	100
750	50	50%	0%	50%	50	5%	95%	0	100

Table 3. Design of experiments—part 2 "temperature variation".

T	Fuel Electrode Supply				Air Electrode Supply			Operating Currents	
	$\dot{Q}$	x_{H_2}	x_{N_2}	x_{H_2O}	$\dot{Q}$	x_{O_2}	x_{N_2}	j0	j1
°C	NL/h	%$_{vol,wb}$	%$_{vol,wb}$	%$_{vol,wb}$	NL/h	%$_{vol,db}$	%$_{vol,db}$	mA/cm^2	mA/cm^2
800	50	97%	0%	3%	50	21%	79%	0	100
750	50	97%	0%	3%	50	21%	79%	0	100
700	50	97%	0%	3%	50	21%	79%	0	100
650	50	97%	0%	3%	50	21%	79%	0	100
600	50	97%	0%	3%	50	21%	79%	0	100

Then, Table 3 shows the test plan with focus on the temperature variation (600–800 °C). For this test series, the reactant gases concentrations and total flow rate do not vary, and the current density levels are standard (0 and 100 mA/cm^2).

3. Results and Discussion

The Kramers–Kronig (KK) test was applied, and relative residuals of both real and imaginary parts were calculated to assess the quality of the acquired AC response [34,35]. The KK relation connects the real and imaginary parts of complex functions, namely the impedance response for the case under investigation. To do this, the AC response must satisfy the three criteria for a good EIS measurement, i.e., linearity, stationarity, and causality [34]. If the relative residuals (both real and imaginary) fall within the ±0.5% range, the AC response is commonly accepted as a good measurement. The KK relative residuals, calculated on an AC response acquired at T = 800 °C, H$_2$ 50 mL min^{-1} (xH$_2$ = 97%), air 50 mL min^{-1} (xO$_2$ = 21%), j = 0 mAcm^{-2}, are shown in Figure S1. Both the real and the imaginary relative residuals are below ± 0.5% in the studied frequency range. Only at 4.5 kHz do the relative residuals of the imaginary part reach their maximum value of 0.3%, which can still be considered a satisfactory value. This phenomenon occurred in the frequency range in which the impedance spectrum intercepts the real axis. This error can be assigned to the unwanted, wire-originated, inductive contribution at high frequency.

3.1. Optimization of the Regularization Parameter

To determine the optimal regularization parameter, DRT functions were calculated by using different λ values: $10^{-1}, 10^{-2}, 10^{-3}$, and 10^{-4}. Then, Nyquist plots were reconstructed from the obtained DRT functions. The DRT functions obtained with different λ and the corresponding Nyquist plot are reported in Figure S2. At high λ values, the DRT functions become smoother, with a loss of information. For instance, the peak at ≈20 Hz completely disappears at λ = 10^{-1}. Furthermore, the Nyquist plot of λ = 10^{-1} does not match with the experimental plot in the low-frequency region. By decreasing the regularization parameters, the DRT function shape improves, giving sharper and more resolved peaks. At λ = 10^{-2} the reconstructed Nyquist plot still does not match the experimental one in the low-frequency region. However, as the regularization parameter decreases, the reconstructed Nyquist improves the shape, giving a good match at λ = 10^{-3}. To better understand the choice of the optimal regularization parameter, relative residuals and pseudo χ^2 were calculated between the experimental and reconstructed Nyquist plots. The relative residuals were calculated by using Equations (1) and (2), while the pseudo χ^2 is obtained with reference to Equation (3). The residuals, as well as the pseudo χ^2 values obtained with different regularization parameters, are shown in Figure S3. With DRT functions calculated with λ = 10^{-1} and 10^{-2}, the relative residuals were not acceptable with high values of the imaginary part in the low-frequency region, in good agreement with the reconstructed Nyquist plot reported in Figure S2b. With λ = 10^{-3}, the residuals graph shows mostly statistical noise with the exception at 5 kHz, which was also previously observed with the KK residuals in Figure S1, probably due to the wire-originated inductivities. With λ = 10^{-4} no significant changes were observed compared with λ = 10^{-3}. At last, the sum of squared

residuals vs. λ was calculated with Relaxis 3 software (Figure S4). As the regularization parameter decreases, the SSR decreases, reaching an asymptote at $\lambda < 10^{-3}$. However, using very low λ values can create meaningless artifact peaks. For this reason, a regularization parameter of $\lambda = 10^{-3}$ was chosen as an optimal value for the DRT function calculation.

3.2. Effect of the Working Temperature: Detection of the Charge-Transfer Process

Since the DRT function is a model-free representation of an AC response and a comparative method, it is useful to consider the physicochemical meaning of the polarization losses. Diffusion processes are mostly dependent on gas feeding changes such as flow rate or composition, while are commonly not affected by the working temperature [36]. On the other hand, charge transfer processes are always thermally activated. For this reason, AC responses were acquired at different working temperatures 600 °C < T < 800 °C with 50 °C steps. The Nyquist plots and the calculated DRT functions are shown in Figure 4. The Nyquist plots (Figure 4a,b) are characterized by four features: (i) a positive shift in the real axis, (ii) a high-frequency inductive feature, (iii) a semicircle in the high/medium-frequency region, and (iv) a semicircle in the low-frequency region. In both cases, at OCV and under a 100 mA cm^{-2} load, the overall impedance and the positive shift in the real axis decrease as the temperature increases. However, the highest contribution to the decreases of the overall impedance is given by the semicircle in the high/medium-frequency region. In contrast, the arc in the low-frequency region was almost unaltered. Their respective DRT functions are given in Figure 4c,d. The DRT functions are characterized by six peaks spread from 10^{-2} Hz up to 104 Hz. The peak P1 at $\approx 10^{-2}$ Hz was only detected at 600 and 650 °C, while the peak P4, located at 103 Hz, is not well resolved, and always overlaps with P3 and P5. The peaks P3, P4 and P6 were not subject to any significant changes during the experiment. The peak P2 had a slight change on the measurement under load; however, the arc in the low-frequency region related to this peak does not show any significant changes in terms of impedance magnitude. In both OCV and under load measurements, the peak P5 was the most subject to the operational temperature changes, decreasing in magnitude and shifting to higher frequencies at higher working temperatures.

The Arrhenius plot of the resistance associated to P5 is hown in Figure 4e. In both cases, at OCV and under load, a linear relationship of $\ln(1/R_{P5})$ vs. 1000/T (K) was found, suggesting that the process related to P5 is thermally activated, i.e., a charge-transfer process [33,37]. Furthermore, P5 shifts to higher characteristics frequency when a load of 100 mA cm^{-2} is applied which can be explained by relation between the charge-transfer resistance and the exchange current in the Butler-Volmer equation as suggested by Caliandro et al. in [27] and Leonide A. in [13].
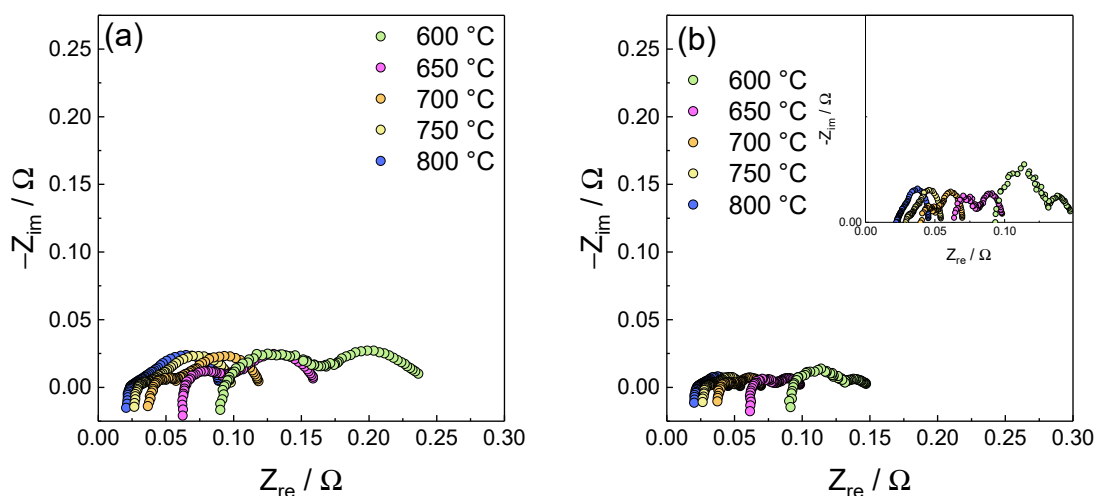

Figure 4. *Cont.*
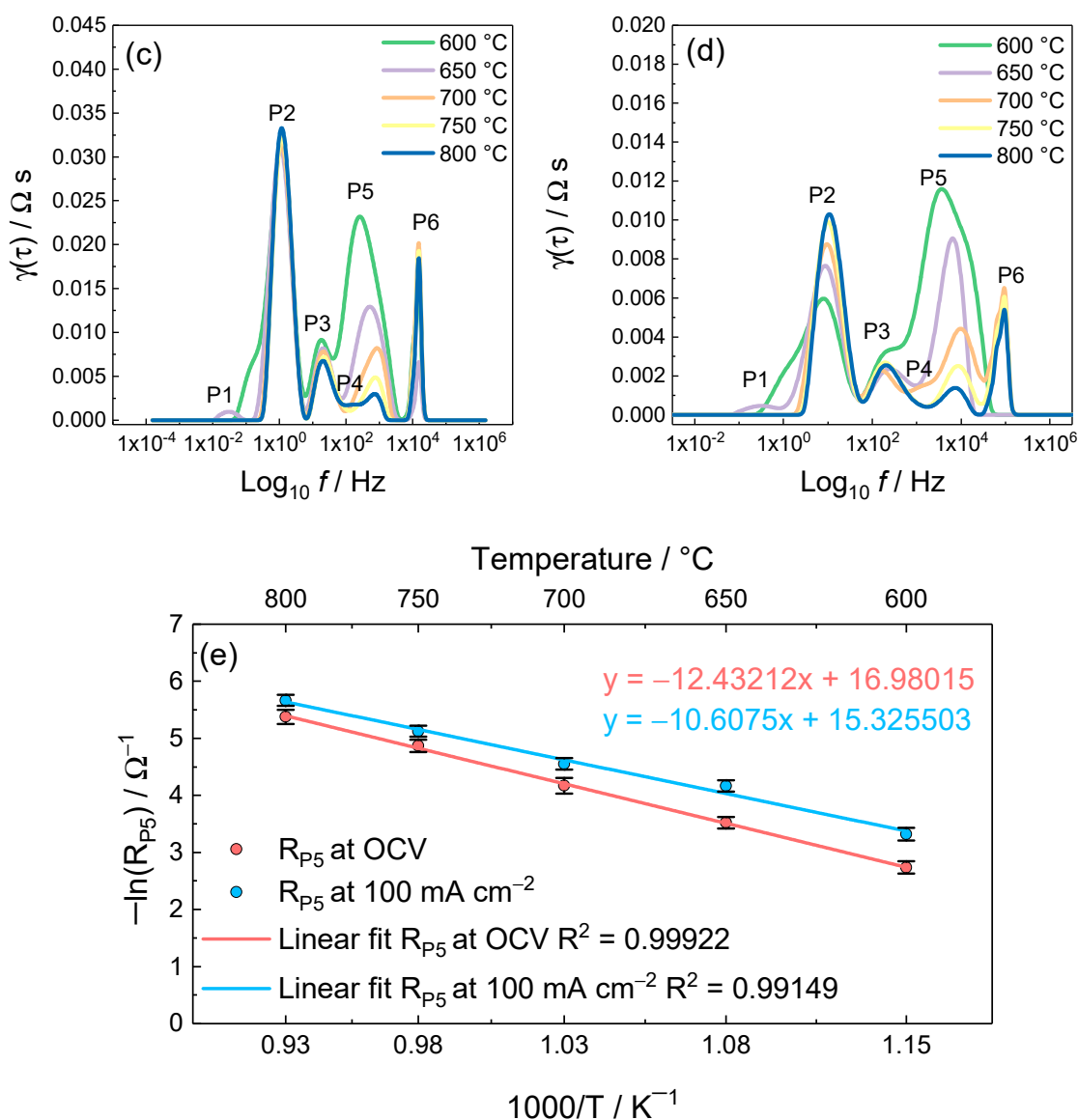
Figure 4. Nyquist plots obtained at different working temperatures at (**a**) OCV and (**b**) under a 100 mA cm^{-2} load. DRT deconvolution at (**c**) OCV and (**d**) under 100 mA cm^{-2} load. (**e**) Arrhenius plot of RP5 with linear fit at both OCV and under 100 mA cm^{-2} load. FE = 50 mL min^{-1} H$_2$ (xH$_2$ = 97%), AE = 50 mL min^{-1} air (xO$_2$ = 21%).

3.3. Effect of Fuel Composition: Detection of the Gas Diffusion Process in the Ni-YSZ Substrate

The effect of fuel composition and flow rate on the impedance response was studied by (i) decreasing the xH$_2$ (24.3% < xH$_2$ < 97%, xH$_2$O = 3%, balanced with N$_2$), and (ii) by increasing the steam content in the fuel (3% < xH$_2$O < 50%). The results obtained at OCV with different xH$_2$ and Q$_{FE}$ are reported in Figure 5.

In all measurements, the peak P1 was not detectable. The peak P2 increased in intensity and shifted to lower frequencies as the xH$_2$ decreased. The peak P3 increases in intensity as the xH$_2$ decreases. The peaks P4, P5, and P6 did not show any dependence on fuel composition and flow rate changes. Since the peaks P2 and P3 were the most subjected to the fuel composition and flow rate changes, it can be assumed that they describe the gas-diffusion in the pores of the Ni-YSZ substrate [13,26], with P2 and P3 being the τ_1 and

τ_2 of a finite length Warburg-type diffusion (FLW). The characteristic time τ_0 of the FLW can be calculated with Equation (4) [26]:

$$\tau_k = \frac{\tau_0}{\pi^2 (k - 0.5)^2}, \; k = 1, 2, 3, \ldots \tag{4}$$
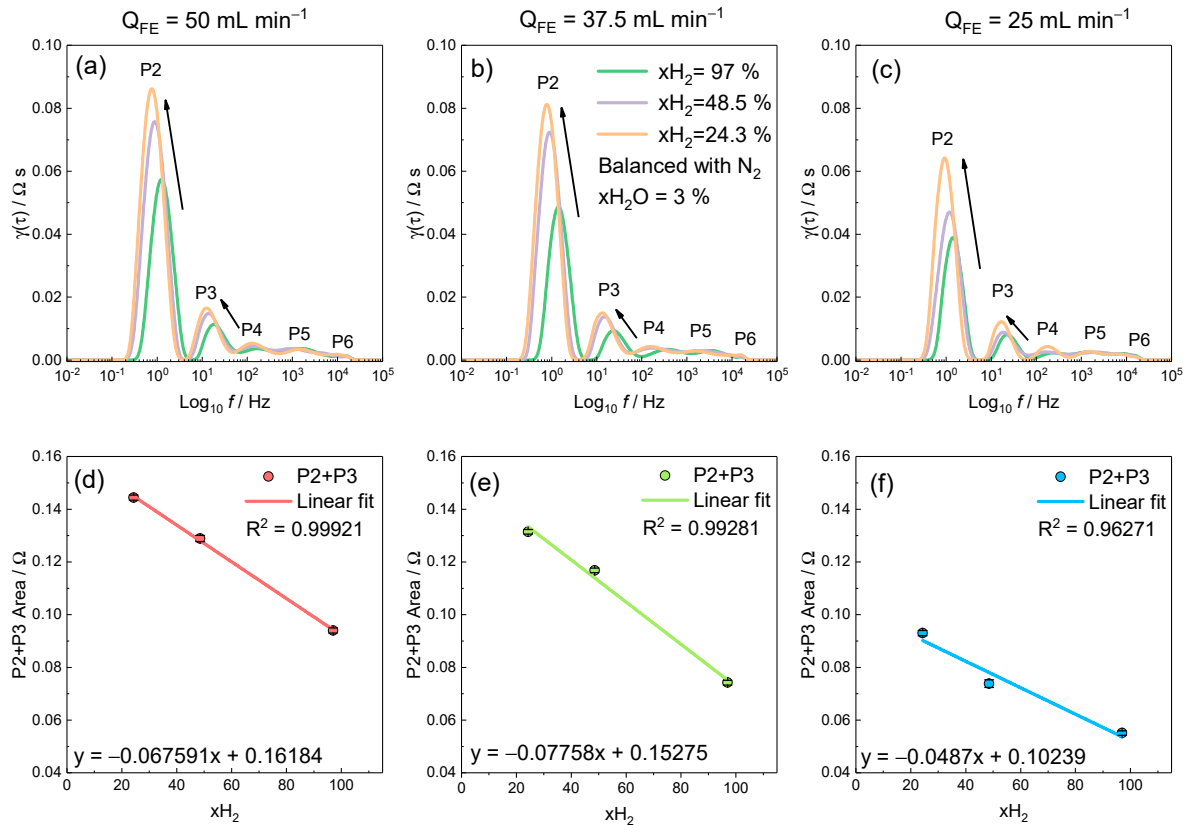
Figure 5. DRT functions of impedance responses obtained at different x_{H2} and Q_{FE}. (**a**) $Q_{FE} = 50$ mL min^{-1}. (**b**) $Q_{FE} = 37.5$ mL min^{-1}. (**c**) $Q_{FE} = 25$ mL min^{-1}. Green line $x_{H2} = 97\%$, purple line $x_{H2} = 48.5\%$, and orange line $x_{H2} = 24.3\%$. P2 + P3 peak area vs. x_{H2} at (**d**) $Q_{FE} = 50$ mL min^{-1}, (**e**) $Q_{FE} = 37.5$ mL min^{-1}, and (**f**) $Q_{FE} = 25$ mL min^{-1} with their respective linear fit. $T = 800\,^{\circ}$C, AE = air 50 mL min^{-1} ($x_{O2} = 21\%$), j = OCV.

By measuring τ_1 (centre point of P2) from the experimental data set, it is possible to calculate τ_0, which can be used during the CNLS-fit as starting parameter for the ECM. In Figure 5d–f, the area of peak P2 + P3 vs. x_{H2} with their respective linear fit is reported. In all three cases, a linear relationship between x_{H2} and the area of P2 + P3 is observed, confirming that the peak can be ascribed to the gas diffusion in the anode support layer. The results with different H_2O content in the fuel are reported in Figure 6. As demonstrated in the literature [7,13,27], the H_2O content in the fuel has a significant impact on the AC response of SOCs, especially on the polarization loss due to mass transport in the anode support layer. As shown in Figure 6a, the peaks P2 and P3 were the most subjected to the increase of H_2O content in the fuel stream. The peak P2 decreased in intensity and shifted to higher relaxation frequencies, while the peak P3 (which is smaller than P2 [26]) disappeared. The peak P1 starts appearing at $x_{H2O} > 25\%$ and was probably overlapped with P2 in the measurement at $x_{H2O} = 3\%$.
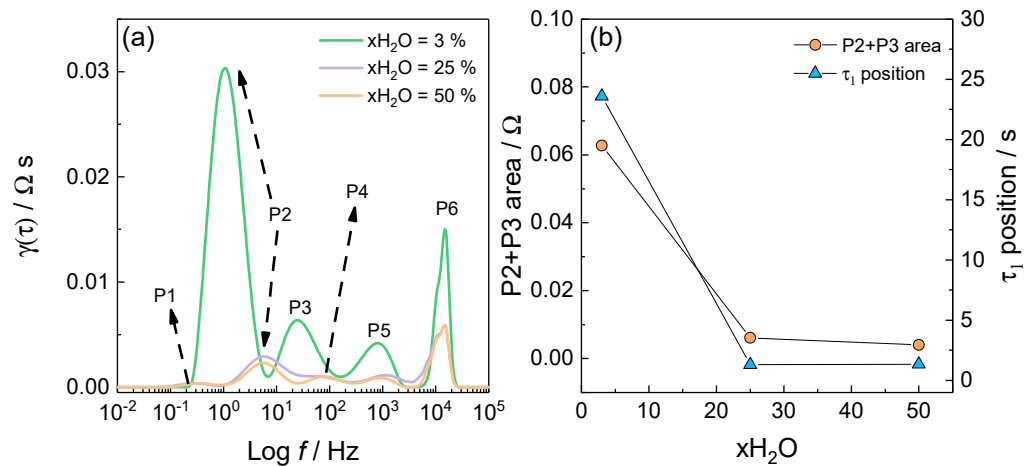
Figure 6. (**a**) DRT functions calculated from AC responses with different H_2O content in the fuel. (**b**) P2 + P3 area and τ_1 position vs. H_2O content in the fuel. T = 750 °C, j = OCV, Q_{FE} = 50 mL min^{-1}, Q_{AE} = 50 mL min^{-1}, and xO_2 = 21%.

The peak P4 overlapped with P3 in the measurement at xH_2O = 3%; however, in the measurement with higher steam content, the peak was better resolved and was not subjected to changes. The peaks P5 and P6 decreased in intensity only during the change from xH_2O = 3% to 25%. The area of peak P2 + P3 and τ_1 vs. the steam content is reported in Figure 6b. Both area and τ_1 decrease as the steam content in the fuel increases, reaching a minimum at xH_2O = 50%. This behaviour was already observed by Caliandro et al. in [27], in which a maximum of the peak area was observed at xH_2O = 5%, for then reaching the minimum at xH_2O = 50%. The evidence observed with different xH_2, fuel flow rate and steam content in the fuel confirm that P2 and P3 are associated with the gas diffusion in the anode support layer with a finite length Warburg-type diffusion. Under OCV conditions, the gas transport in the porous anode substrate can be described by the Stefan-Maxwell multicomponent diffusion [38,39]. Accordingly, the gas diffusion in the anode support layer can also be represented as (Equation (5)) in the case of a diffusion with a bicomponent mixture (RP2 + P3 vs. xH_2O, fuel components H_2 and H_2O), and as (Equation (6)) in the case of a tricomponent mixture (RP2 + P3 vs. xH_2, fuel components H_2, N_2, and H_2O):

$$R_W = \left(\frac{RT}{2F}\right)^2 \frac{l}{PD_{H_2, H_2O}} \frac{\kappa}{\varphi}\left(\frac{1}{pH_2} + \frac{1}{pH_2O}\right) \tag{5}$$

$$R_W = \left(\frac{RT}{2F}\right)^2 \frac{l}{P} \frac{\kappa}{\varphi}\left[\frac{1}{x_{H_2O}}\left(\frac{x_{H_2}}{D_{H_2,H_2O}} + \frac{x_{H_2O}}{D_{H_2,H_2O}} + \frac{x_{N_2}}{D_{H_2O,N_2}}\right) + \frac{1}{x_{H_2}}\left(\frac{x_{H_2}}{D_{H_2,H_2O}} + \frac{x_{H_2O}}{D_{H_2,H_2O}} + \frac{x_{N_2}}{D_{H_2,N_2}}\right)\right] \tag{6}$$

where R, T, F, l, P are the gas constant, the working temperature, the Faraday constant, the thickness of the anode substrate, and the atmosphere pressure. κ and φ are the tortuosity factor and the porosity, respectively, while the xi is the molar fraction of the i species. $D_{i,j}$ is the binary diffusion coefficient in void space for the species i and j [38]. In the case of the bicomponent diffusion (H_2 and H_2O), by using Equation (5), as the steam content (xH_2O) is increased, the resistance associated with the diffusion decreases. On the other hand, in the case of a ternary diffusion, as the N_2 content is increased with xH_2O being constant at 3%, the resistance associated with the diffusion increases.

3.4. Effect of Air Electrode Gas Composition

Measurements at different xO_2 (balanced with N_2) were carried out to shed a light on the cathode processes. To properly assess and unravel the cathode-related features, impedance spectra were acquired not only at different xO_2, but also in the presence of

H_2O in the fuel to decrease the polarization due to the fuel transport in the anode support layer and, thus, uncover the peaks related to the air electrode. In Figure 7, the DRT functions obtained at different xO_2 with increasing steam concentration in the fuel electrode are shown.
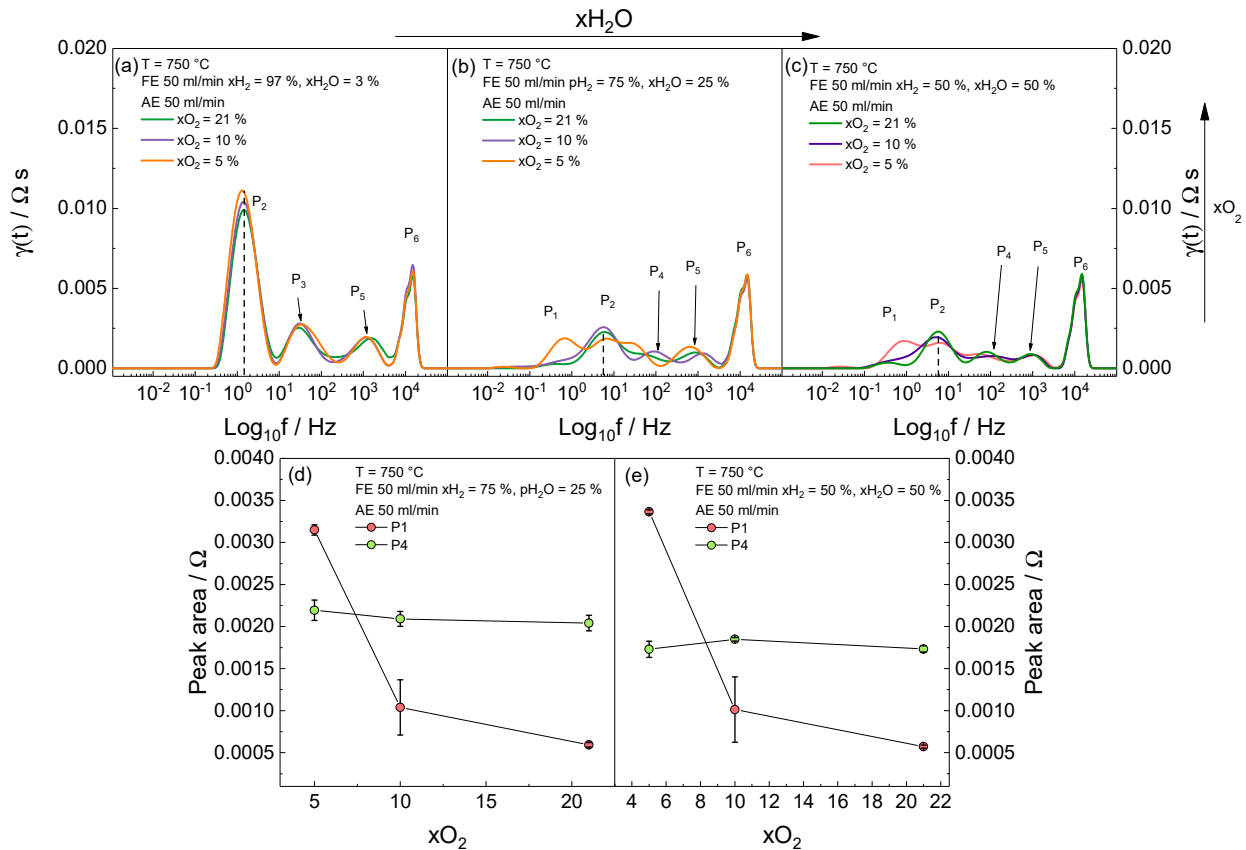

Figure 7. DRT functions obtained at (**a**) xH_2O = 3%, (**b**) xH_2O = 25%, and (**c**) xH_2O = 50%. P1 and P4 area vs. xO_2 at (**d**) xH_2O = 25% and (**e**) xH_2O = 50% in the fuel. T = 750 °C, Q_{FE} = 50 mL min^{-1}, and Q_{AE} = 50 mL min^{-1}. Green line xO_2 = 21%, purple line xO_2 = 10%, and orange line xO_2 = 5%.

The DRT functions obtained with xH_2O = 3% in the fuel electrode are characterized by the two peaks P2 and P3, which are related to the gas transport in the anode support layer, P5, which is due to the charge-transfer processes, and P6. As the xO_2 in the air electrode decreases, no substantial changes occur in the DRT functions, and the signals related to the cathode are probably still covered by the peaks P2 and P3. As the steam content in the fuel increases to xH_2O = 25% and 50% (Figure 7b,c), the peak P2 shift to slightly higher relaxation frequencies and decreases in intensity, while the peak P3 disappear. As H_2O is introduced in the fuel electrode, the peaks P1 and P4, centred at ≈0.5 Hz and ≈100 Hz, respectively, unravel. As shown in Figure 7b,c, the intensity of P1 increases as xO_2 in the air electrode decreases. This behaviour is also observed in Figure 7d,e, with the fit of the area of P1 vs. xO_2, in which an increase of the area related to P1 is detected at low xO_2. For this reason, P1 was assigned to the gas diffusion in the air electrode pores. As shown in Figure 7b–e, P4 has negligible changes of the area with the variation of xO_2. Only at xH_2O = 25% and xO_2 = 5% the peak shifted from 100 Hz down to 30 Hz. As discussed in [13,28,40], the polarization related to the peak P4 can be ascribed to the oxygen surface exchange kinetics of LSCF as well as the diffusion of O^{2-} through the LSCF bulk, and therefore it has an almost negligible dependence on xO_2. The peak P6 does not show any dependence with the explored operating parameters, and since it falls in the same frequency range in which high relative residuals were observed with the Kramers–Kronig test, the authors suggest that the peak is related to an experimental error.

3.5. Equivalent Circuit Model CNLS-Fit

As described in Section 2.3, the AC responses were fitted with the following ECM $LR_{el}(R_{ct}Q)GW_{FLW}$. An inductor element was used to model the inductive feature present in the high-frequency region. A resistor R_{el} was used to model the electrolyte resistance, graphically represented as the positive shift in the high-frequency region. The arc in the high-to-middle frequency region was fitted with a resistor-CPE parallel ($R_{ct}Q$), modelling the charge-transfer resistance (P5) and its related capacitance. The peak P4, related to the oxygen surface exchange and diffusion of O^{2-} in the LSCF bulk, was modelled with a Gerischer element G, while the gas diffusion in the anode substrate (P2 and P3) was modelled with a finite length Warburg WFLW. The ECM, as well as an experimental spectrum with the CNLS-fit, are shown in Figure 8a.

The CNLS-fit with the ECM adopted resulted in a good fit of the experimental spectrum, with both relative imaginary and real residuals being lower than 0.5% (Figure 8b). In Figure 8c, the Arrhenius plot of the resistance associated to the charge-transfer process is reported. As shown in Figure 4e, a linear relationship between the $\ln(R^{-1})$ and $1000/T$ was found, suggesting a thermally activated behaviour [40]. The activation energy was calculated by using the slope of the linear fit and Arrhenius equation [40] (Equation (7), where E_a is the activation energy, k_b is the Boltzmann constant, and A is the pre-exponential factor). The activation energies obtained by both DRT and CNLS-fit are reported in Table 4.

$$\ln\left(\frac{1}{R_{ct}}\right) = A - \frac{E_a}{k_b T} \tag{7}$$

Table 4. Activation energies calculated from CNLS-fit and DRT.

Technique	E_a	
	j = OCV	j = 100 mA cm^{-2}
DRT	$E_a = 1.07132 \pm 0.0851$ eV	$E_a = 0.90674 \pm 0.07104$ eV
CNLS-fit	$E_a = 1.09029 \pm 0.19247$ eV	$E_a = 0.76992 \pm 0.03505$ eV

Similar activation energies were obtained with both methods, with values ≈ 1.1 eV at OCV and 0.85 eV at 100 mA cm^{-2}, which is in agreement with literature results [13,27,41]. In Figure 8d, the R_{FLW} and τ_{FLW} vs. xH_2O plot is reported. A similar behaviour to that observed with DRT in Figure 6b is noticed, with a decrease of the resistance and the characteristic time as the steam content is increased. On the other hand, as observed in Figure 5d–f, the resistance associated with the gas diffusion in the anode substrate increases with increasing N_2 content in the fuel. In both R_{FLW} vs. xH_2O, and R_{FLW} vs. xN_2, similar values of R_{FLW} and slopes (in the case of R_{FLW} vs xN_2) were obtained with both DRT and ECM CNLS-fit.
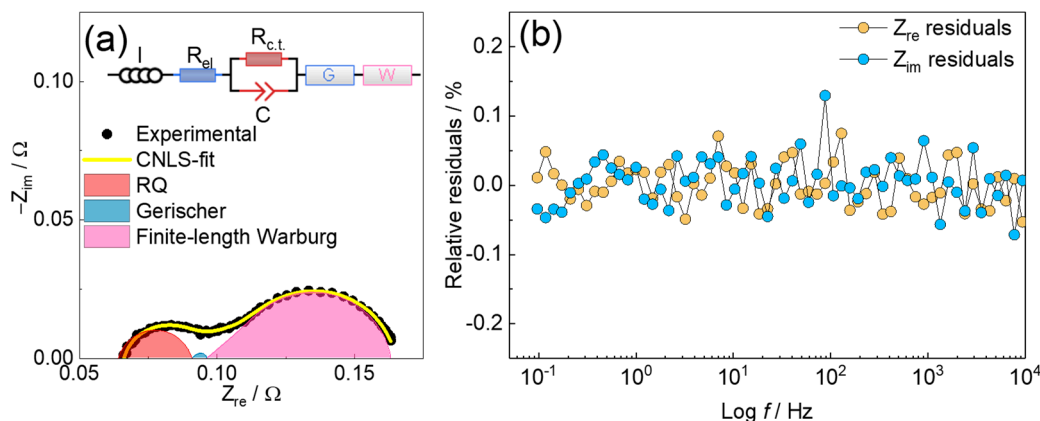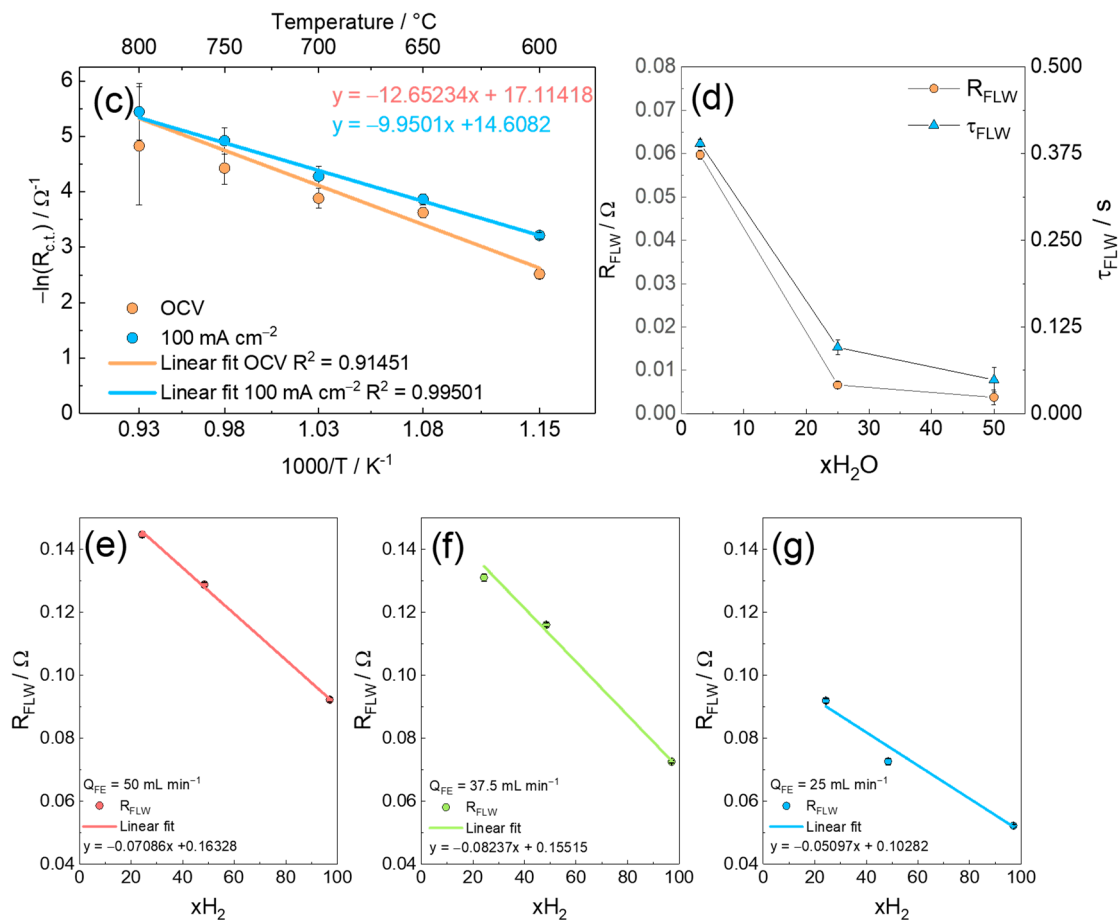

Figure 8. *Cont.*

Figure 8. (**a**) Nyquist plot, fit results and ECM, (**b**) relative residuals of the CNLS-fit result. AC response in (**a**) and (**b**) was acquired at T 600 °C, Q_{FE} = 50 mL min^{-1} xH_2 = 97%, xO_2 = 21%, and j = OCV. (**c**) Arrhenius plot ln($R_{c.t.}^{-1}$) vs. 1000/T with linear fit. R_{FLW} vs. (**d**) xH_2O and (**e**–**g**) vs. xH_2 (xH_2O = 3%, balanced with N_2). The latter were acquired with a Q_{FE} of (**e**) 50 mL min^{-1}, (**f**) 37.5 mL min^{-1}, and (**g**) 25 mL min^{-1}, T = 800 °C, j = OCV.

4. Conclusions

In this paper, the complete methodology for the identification of early-stage degradation effects in commercial-sized SOCs is presented and validated through tests performed on single cells framed with steel interconnects as in stacks. The methodology is based on electrochemical impedance measurement and ex post data analysis. The main contributions to the cell impedance are identified as being charge transfer (DRT peak at f = 10^3–10^4 Hz), oxygen surface exchange and diffusion in the bulk LSCF (DRT peak at f = 10^2–10^3 Hz), and gas diffusion in the fuel electrode (double DRT signal in the frequency range 1–100 Hz). The results are validated using the ECM methodology, implementing an $LR_{el}(R_{ct}Q)GWFLW$ circuit. This work provides the basis for a real-time operando degradation diagnosis tool, with a wide room for implementation in SOC R&D, as well as standard operation performance monitoring.

Abbreviations

AC	Alternate Current
AEL	Alkaline Electrolysers
AFC	Alkaline Fuel Cells
CNLS	Complex Non-linear Least Square
DRT	Distribution of Relaxation Times
ECM	Equivalent Circuit Model
EIS	Electrochemical Impedance Spectroscopy
KK	Kramers–Kronig
MCFC	Molten Carbonate Fuel Cells
PAFC	Phosphoric Acid Fuel Cells
PEME	Polymer Electrolyte Membrane Electrolysers
PEMFC	Polymer Electrolyte Membranes Fuel Cells
SOC	Solid Oxide Cells
SOE	Solid Oxide Electrolysers
SOFC	Solid Oxide Fuel Cell
XRD	X-ray Diffraction Analysis

References

1. Victoria, M.; Zhu, K.; Brown, T.; Andresen, G.B.; Greiner, M. The role of storage technologies throughout the decarbonisation of the sector-coupled European energy system. *Energy Convers. Manag.* **2019**, *201*, 111977. [CrossRef]
2. European Commission. *Communication from the Commission to the European Parliament, the European Council, the Council, the European Economic and Social Committee and the Committee of the Regions the European Green Deal*; European Commission: Brussels, Belgium, 2020; pp. 106–117.
3. Sunfire takes significant steps to clean energy on demand using solid oxide technology. *Fuel Cells Bull.* **2016**, *2016*, 12–14. [CrossRef]
4. Keçebaş, A.; Kayfeci, M.; Bayat, M. Electrochemical hydrogen generation. In *Solar Hydrogen Production*; Elsevier: Amsterdam, The Netherlands, 2019; pp. 299–317.

5. Baldinelli, A.; Barelli, L.; Bidini, G.; Di Cicco, A.; Gunnella, R.; Minicucci, M.; Trapananti, A. Advancements regarding in-operando diagnosis techniques for solid oxide cells NiYSZ cermets. In *AIP Conference Proceedings*; American Institute of Physics Inc.: College Park, MD, USA, 2019; Volume 2191, p. 020012.

6. Shirbhate, S.; Gaikwad, V.; Acharya, S. Oxygen vacancies disordering and oxy-ion diffusion mechanism in doped ceria electrolytes under IT-SOFC operating conditions. *J. Solid State Electrochem.* **2022**, *26*, 133–148. [CrossRef]

7. Dierickx, S.; Weber, A.; Ivers-Tiffée, E. How the distribution of relaxation times enhances complex equivalent circuit models for fuel cells. *Electrochim. Acta* **2020**, *355*, 136764. [CrossRef]

8. Schmidt, J.P.; Berg, P.; Schönleber, M.; Weber, A.; Ivers-Tiffée, E. The distribution of relaxation times as basis for generalized time-domain models for Li-ion batteries. *J. Power Source* **2013**, *221*, 70–77. [CrossRef]

9. Chen, X.; Li, L.; Liu, M.; Huang, T.; Yu, A. Detection of lithium plating in lithium-ion batteries by distribution of relaxation times. *J. Power Source* **2021**, *496*, 229867. [CrossRef]

10. Goldammer, E.; Kowal, J. Determination of the Distribution of Relaxation Times by Means of Pulse Evaluation for Offline and Online Diagnosis of Lithium-Ion Batteries. *Batteries* **2021**, *7*, 36. [CrossRef]

11. Kim, D.; Muckley, E.S.; Creange, N.; Wan, T.H.; Ann, M.H.; Quattrocchi, E.; Vasudevan, R.K.; Kim, J.H.; Ciucci, F.; Ivanov, I.N.; et al. Exploring Transport Behavior in Hybrid Perovskites Solar Cells via Machine Learning Analysis of Environmental-Dependent Impedance Spectroscopy. *Adv. Sci.* **2021**, *8*, 2002510. [CrossRef]

12. Hernández-Balaguera, E.; Romero, B.; Najafi, M.; Galagan, Y. Analysis of Light-Enhanced Capacitance Dispersion in Perovskite Solar Cells. *Adv. Mater. Interfaces* **2022**, *9*, 2102275. [CrossRef]

13. Leonide, A.; Sonn, V.; Weber, A.; Ivers-Tiffée, E. Evaluation and Modeling of the Cell Resistance in Anode-Supported Solid Oxide Fuel Cells. *J. Electrochem. Soc.* **2007**, *155*, B36. [CrossRef]

14. Osinkin, D.A. An approach to the analysis of the impedance spectra of solid oxide fuel cell using the DRT technique. *Electrochim. Acta* **2021**, *372*, 137858. [CrossRef]

15. Sumi, H.; Shimada, H.; Yamaguchi, Y.; Yamaguchi, T.; Fujishiro, Y. Degradation evaluation by distribution of relaxation times analysis for microtubular solid oxide fuel cells. *Electrochim. Acta* **2020**, *339*, 135913. [CrossRef]

16. Yan, Y.; Fang, Q.; Blum, L.; Lehnert, W. Performance and degradation of an SOEC stack with different cell components. *Electrochim. Acta* **2017**, *258*, 1254–1261. [CrossRef]

17. Subotić, V.; Königshofer, B.; Juričić, Đ.; Kusnezoff, M.; Schröttner, H.; Hochenauer, C.; Boškoski, P. Detailed insight into processes of reversible solid oxide cells and stacks using DRT analysis. *Energy Convers. Manag.* **2020**, *226*, 113509. [CrossRef]

18. Groetsch, C.W. The Theory of Tikhonov Regularization for Fredholm Equations of the First Kind (C. W. Groetsch). *Siam Rev.* **1984**, *28*, 116–118.

19. Horlin, T. Deconvolution and maximum entropy in impedance spectroscopy of noninductive systems. *Solid State Ion.* **1998**, *107*, 241–253. [CrossRef]

20. Hörlin, T. Maximum entropy in impedance spectroscopy of non-inductive systems. *Solid State Ion.* **1993**, *67*, 85–96. [CrossRef]

21. Boukamp, B.A. Fourier transform distribution function of relaxation times: Application and limitations. *Electrochim. Acta* **2015**, *154*, 35–46. [CrossRef]

22. Boukamp, B.A.; Rolle, A. Analysis and Application of Distribution of Relaxation Times in Solid State Ionics. *Solid State Ion.* **2017**, *302*, 12–18. [CrossRef]

23. Saccoccio, M.; Wan, T.H.; Chen, C.; Ciucci, F. Optimal Regularization in Distribution of Relaxation Times applied to Electrochemical Impedance Spectroscopy: Ridge and Lasso Regression Methods-A Theoretical and Experimental Study. *Electrochim. Acta* **2014**, *147*, 470–482. [CrossRef]

24. Wan, T.H.; Saccoccio, M.; Chen, C.; Ciucci, F. Influence of the Discretization Methods on the Distribution of Relaxation Times Deconvolution: Implementing Radial Basis Functions with DRTtools. *Electrochim. Acta* **2015**, *184*, 483–499. [CrossRef]

25. Staffolani, A.; Baldinelli, A.; Barelli, L.; Bidini, G.; Nobili, F. Early-Stage Detection of Solid Oxide Cells Anode Degradation by Operando Impedance Analysis. *Processes* **2021**, *9*, 848. [CrossRef]

26. Boukamp, B.A. Derivation of a Distribution Function of Relaxation Times for the (fractal) Finite Length Warburg. *Electrochim. Acta* **2017**, *252*, 154–163. [CrossRef]

27. Caliandro, P.; Nakajo, A.; Diethelm, S.; Van Herle, J. Model-assisted identification of solid oxide cell elementary processes by electrochemical impedance spectroscopy measurements. *J. Power Sources* **2019**, *436*, 226838. [CrossRef]

28. Hong, J.; Bhardwaj, A.; Bae, H.; Kim, I.; Song, S.-J. Electrochemical Impedance Analysis of SOFC with Transmission Line Model Using Distribution of Relaxation Times (DRT). *J. Electrochem. Soc.* **2020**, *167*, 114504. [CrossRef]

29. Dierickx, S.; Joos, J.; Weber, A.; Ivers-Tiffée, E. Advanced impedance modelling of Ni/8YSZ cermet anodes. *Electrochim. Acta* **2018**, *265*, 736–750. [CrossRef]

30. Grolig, J.G.; Alnegren, P.; Froitzheim, J.; Svensson, J.-E. Copper Iron Conversion Coating for Solid Oxide Fuel Cell Interconnects. *J. Power Source* **2015**, *297*, 534–539. [CrossRef]

31. Baldinelli, A.; Staffolani, A.; Bidini, G.; Barelli, L.; Nobili, F. An extensive model for renewable energy electrochemical storage with Solid Oxide Cells based on a comprehensive analysis of impedance deconvolution. *J. Energy Storage* **2020**, *33*, 102052. [CrossRef]

32. Boukamp, B.A. A Nonlinear Least Squares Fit procedure for analysis of immittance data of electrochemical systems. *Solid State Ion.* **1986**, *20*, 31–44. [CrossRef]

33. Barsoukov, E.; Ross Macdonald, J. *Impedance Spectroscopy: Theory, Experiment, and Applications*, 3rd ed.; John Wiley & Sons, Inc.: Hoboken, NJ, USA, 2018. [CrossRef]

34. Klotz, D.; Weber, A.; Ivers-Tiffée, E. Practical Guidelines for Reliable Electrochemical Characterization of Solid Oxide Fuel Cells. *Electrochim. Acta* **2017**, *227*, 110–126. [CrossRef]

35. Boukamp, B.A. A Linear Kronig-Kramers Transform Test for Immittance Data Validation. *J. Electrochem. Soc.* **1995**, *142*, 1885–1894. [CrossRef]

36. Hayd, J.; Ivers-Tiffée, E. Detailed Electrochemical Study on Nanoscaled La 0.6 Sr 0.4 CoO 3-δ SOFC Thin-Film Cathodes in Dry, Humid and CO 2 -Containing Atmospheres. *J. Electrochem. Soc.* 2013; 160, F1197–F1206. [CrossRef]

37. Arrhenius, S. Über die Reaktionsgeschwindigkeit bei der Inversion von Rohrzucker durch Säuren. *Z. Phys. Chem.* **1889**, *4*, 226–248. [CrossRef]

38. Zhang, Y.; Chen, Y.; Chena, F. In-situ quantification of solid oxide fuel cell electrode microstructure by electrochemical impedance spectroscopy. *J. Power Source* **2015**, *277*, 277–285. [CrossRef]

39. Pisani, L. Multi-component gas mixture diffusion through porous media: A 1D analytical solution. *Int. J. Heat Mass Transf.* **2008**, *51*, 650–660. [CrossRef]

40. Arrhenius, S. Über die Dissociationswärme und den Einfluss der Temperatur auf den Dissociationsgrad der Elektrolyte. *Z. Phys. Chem.* **1889**, *4*, 96–116. [CrossRef]

41. Papurello, D.; Menichini, D.; Lanzini, A. Distributed relaxation times technique for the determination of fuel cell losses with an equivalent circuit model to identify physicochemical processes. *Electrochim. Acta* **2017**, *258*, 98–109. [CrossRef]